



Scratch induced deformation behavior of hafnium based bulk metallic glass at multiple load scales



Debrupa Lahiri^a, Jeffrey Karp^a, Anup K. Keshri^a, Cheng Zhang^a, George S. Dulikravich^b, Laszlo J. Kecskes^c, Arvind Agarwal^{a,*}

^a Nanomechanics and Nanotribology Laboratory, Mechanical and Materials Engineering, Florida International University, Miami, FL 33174, USA

^b MAIDROC, Mechanical and Materials Engineering, Florida International University, Miami, FL 33174, USA

^c US Army Research Laboratory, Aberdeen Proving Ground, MD 21005, USA

ARTICLE INFO

Article history:

Received 28 September 2014

Received in revised form 6 December 2014

Accepted 7 December 2014

Available online xxxx

Keywords:

Bulk metallic glass;

Hafnium;

Multi-scale scratch behavior;

Shear band structure;

Free volume;

Strain hardening

ABSTRACT

The scratch induced deformation behavior of Hafnium based bulk metallic glass (BMG) at *micro*- and *macro*-load scales is reported in this study. The micro-scratch deals with a normal load range of 1000–8000 μN , whereas the macro-scale scratches are made with a normal load reaching up to 5 N. Increase in the load beyond 2000 μN changes the deformation mechanism from plowing to fracture and chipping. The plastic strain is mostly accommodated by shear band formation with a significant amount of free volume generation. A change in the strain rate helps in the nucleation of shear bands and prevents fracture and chipping in the case of micro-scratches made at ramp loading as compared to constant load. Higher strain rate and heat generation in the track causes increased strain hardening in macro-scratch, which could be attributed to increased probability of nano-crystallization. Complex shear band structure is evolved during scratching, which is attributed to the mixed type of loading, consisting of compressive normal load and lateral shear load across scratch-track.

© 2014 Elsevier B.V. All rights reserved.

1. Introduction

Bulk metallic glasses (BMGs) are known for their high fracture strength, low elastic limit, and low plasticity. But, the shear band which forms during deformation introduces failure surfaces along oblique planes relative to the loading axis. This ‘self-sharpening’ behavior in BMGs occurs during dynamic impact as well. This phenomenon is the key for efficient performance as kinetic energy penetrators [1,2]. Hf based bulk metallic glasses (BMG) have been proposed as potential candidates for kinetic energy penetrators due to the high density of Hf, which makes the penetrators more effective [1,2]. A few studies have also been carried out on Hf based alloys to correlate their glass forming ability with deformation and mechanical behavior [1–8].

Bulk metallic glasses have also shown their potential as coatings in dry bearings for use in the outer space [9–11], hard facing alloys, wear resistant coatings for sensors, medical implants, and magnetic heads [9,12]. These applications introduce sliding contact on BMG surfaces, which demands an understanding of their tribological behavior. The machining of BMGs into the final components also uses a single-point tool where deformation conditions can be closely mimicked by scratch experiments [13]. Literature available on micro- and macro-scale scratch studies on Cu, Ni, Zr and Mg based BMGs reveals several aspects

of deformation and failure [12–20]. Coefficient of friction (COF) increases with the applied normal load both at micro- and macro-scales [12,14–16]. But, scratch velocity does not have any effect on the COF [12]. The scratch (wear) resistance of BMGs increases with the hardness [17,19], but does not follow a linear relationship, as in Archard's equation [19]. A change in the wear mode is observed from rubbing and plowing to cutting with an increasing normal load for soft Mg-based BMGs [18]. In situ micro-scratching of Fe-based BMG revealed a transition from ductile plowing to shear band formation and serrated-chipping with an increasing load [20]. Thus, it is very difficult to predict tribological behavior for a certain BMG composition by deriving the similar principle from another BMG. Nevertheless, few commonalities are found in scratch behavior of BMGs. The deformation during scratching is mostly accommodated by shear bands [13,16,17,20]. Higher load causes formation of wider shear bands to accommodate larger deformation [13,20]. A higher scratch velocity leads to finer shear bands which are caused by the activation of multiple shear bands simultaneously to accommodate the applied strain quickly [17]. A study by Maddala et al. [9] on $\text{Cu}_{50}\text{Hf}_{41.5}\text{Al}_{8.5}$ (closest BMG composition to the alloy used in this study) reported tribological behavior in as-cast and annealed samples under sliding wear condition in ball-on-disk wear mode. Wear resistance is found to linearly increase with devitrification, due to formation of nanocrystallites [9]. The wide variation in tribological behavior of bulk metallic glasses is due to their unique structure, which is further complicated by different loading conditions.

* Corresponding author.

E-mail address: agarwala@fiu.edu (A. Agarwal).

Tribological damage generally starts at lower (nano/micro) scale on the surface and aggravates to a macro-scale leading to failure. Thus, it is also important to analyze the tribological behavior at different length scales to fully understand the surface failure mechanism.

Based on the abovementioned scenario, the aim of the present study is to understand the scratch induced deformation behavior of Hf-based BMG, at different modes (*constant* vs. *ramp*) and magnitudes (*micro-Newton* vs. *Newton*) of loading. Microstructural alterations are correlated with the scratch based deformation behavior of Hf-BMG. The formation of shear bands as a result of loading type is analyzed to understand the specific arrangement of the shear bands at the bank/edge of the scratch groove. It is emphasized that scratch induced deformation behavior of Hf-based BMG has never been reported in the literature.

2. Experimental procedures

The Hf-based BMG alloy was prepared by mixing the 99.99% pure elements (Hf, Cu, Nb, Ni and Al) and arc melting them in a Ti-gettered argon atmosphere ($\sim 5 \times 10^4$ Pa). The ingot obtained was melted several times in order to enhance its homogeneity. Further, the arc melted ingot was re-melted and quenched into rod form ($\varnothing = 3$ mm) and was prepared by suction casting it into a copper mold. The alloy used for this study was of the following composition (atomic %): Hf-46.3; Cu-28.2; Ni-13.9; Al-6.2; and Nb-5.4 (referred as Hf-BMG hereafter).

X-ray diffraction (XRD) was carried out using Cu K α ($\lambda = 1.542$ Å) radiation in a Siemens D-5000 X-ray diffractometer operating at 40 kV and 40 mA. A scan rate of $0.2^\circ/\text{min}$ was used. The transmission electron microscope (TEM) sample was prepared by focused ion beam (FIB) milling technique. A Philips/FEI Tecnai F30 high resolution transmission electron microscope (HRTEM), operating at an accelerating voltage of 300 kV, was used to study the BMG sub-structure and capture the selected area diffraction pattern. Glass transition temperature T_g , and melting temperature, T_m , were measured using SDTQ600 (TA Instruments, New Castle, DE). The differential scanning calorimetry (DSC) curve was analyzed from 50°C to 1200°C at a scan rate of $20^\circ\text{C}/\text{min}$ in an argon environment.

Micro-scratch studies were carried out using the 2D scratching module of a Hysitron Triboindenter TI-900. A pyramidal diamond Berkovich probe with a 100 nm tip radius was used for making the scratches. Scratches were made with both *constant* and *ramp* normal loads. The constant loads used were 2000, 4000, or 8000 μN , whereas the ramped scratches were made at an increasing normal loading rate of $80 \mu\text{N} \cdot \text{s}^{-1}$ in the range of 0–8000 μN . All scratches were 10 μm long and made with a lateral displacement rate of $1 \mu\text{m} \cdot \text{s}^{-1}$. The surface profile of the scratch grooves was captured immediately after each scratch, using the scanning probe microscope (SPM) integrated in the triboindenter. A CSM Instrument NanoScratch Tester with a high load cantilever and a 50 μm cono-spherical diamond indenter was used to perform the macro-scratches in the ramp loading mode with a normal load range of 0–5 N. The scratches were 1.5 mm long and performed at a lateral displacement rate of $8.33 \mu\text{m} \cdot \text{s}^{-1}$ and at an increasing normal loading rate of $\sim 30 \text{ mN} \cdot \text{s}^{-1}$. Surface profile of the bank of the scratch was obtained using the SPM. Three or more scratches were made in each condition. All the error values reported in the plots and tables are based on the variations shown amongst these three scratches in each condition.

A JEOL JSM-6330F field emission scanning electron microscope, operating at 15 kV, was used to observe the macro- and micro-scratches. ImageJ software [21] was used for a quantitative analysis of the micro-structural features.

3. Results and discussion

3.1. Structural characterization of the Hf-based BMG

Fig. 1a shows the XRD pattern of the Hf-based BMG alloy. The pattern shows a broad peak at a 2θ range of ~ 35 – 45° , which is the signature

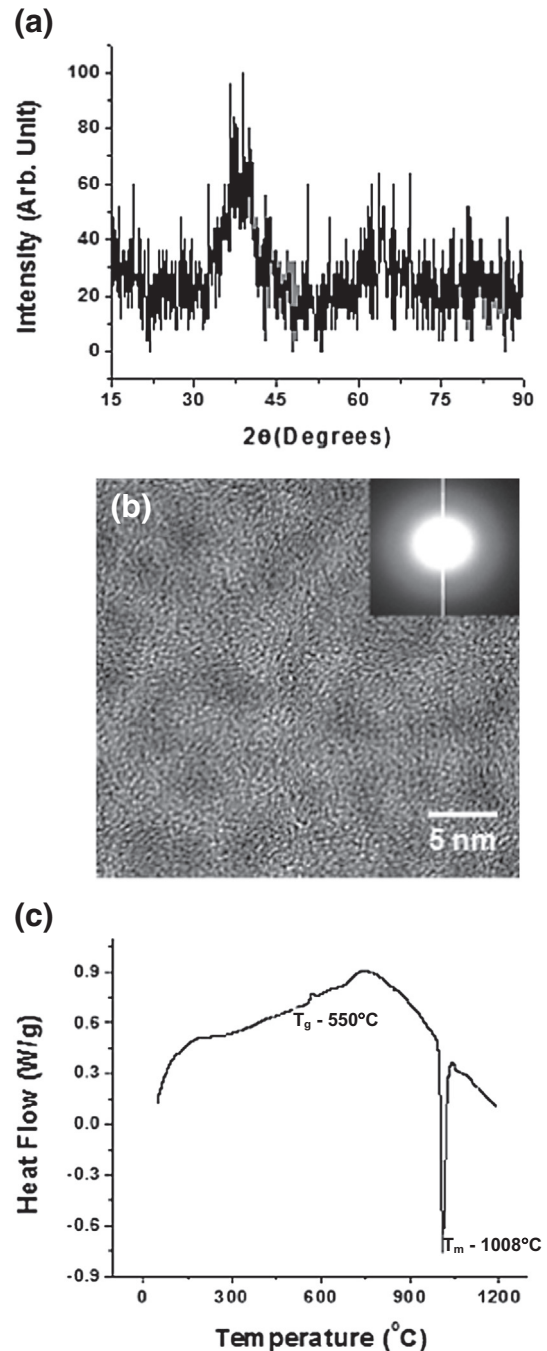


Fig. 1. (a) X-ray diffraction pattern of Hf based BMG; (b) HRTEM image with selected area diffraction pattern as inset and (c) DSC plot for Hf-BMG.

of amorphous structure at bulk scale. Fig. 1b provides high resolution TEM image of Hf-BMG at nano-scale. The absence of lattice fringes and crystalline structure in Fig. 1b indicates the amorphous structure. Selected area diffraction pattern, presented as an inset in Fig. 1b also shows the signature of amorphous structure without any diffraction spots. Fig. 1c presents the DSC curve with an exothermic signal followed by the glass transition. T_g is assessed to be $\sim 550^\circ\text{C}$. The devitrification temperature (T_X) is found to be 570°C at the onset of the crystallization peak.

3.2. Micro-scratch behavior: constant load

Fig. 2 shows the results from the micro-scratch tests performed at constant normal loads of 2000, 4000, and 8000 μN . This is a composite

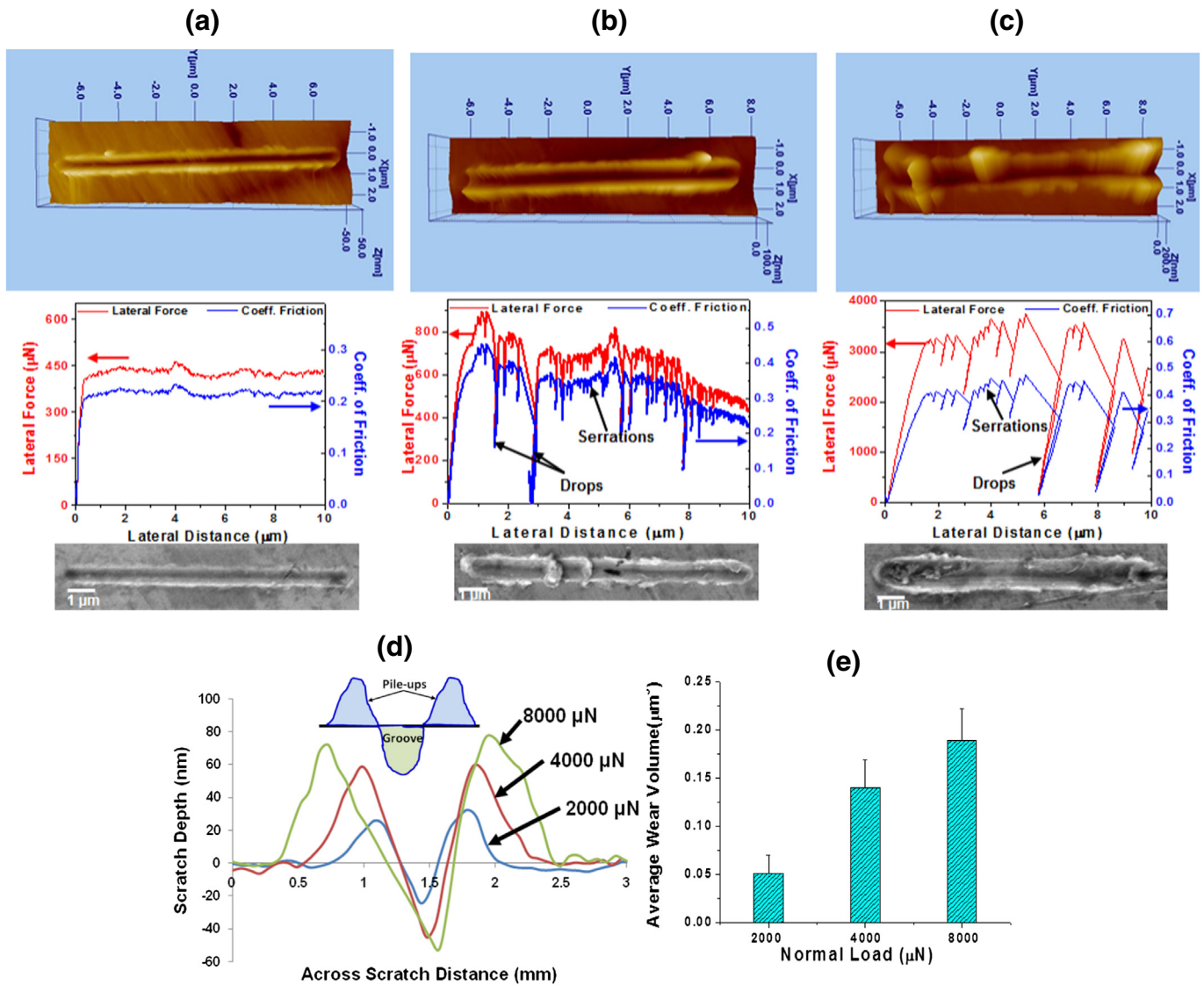


Fig. 2. SPM images, lateral force and coefficient of friction vs. scratch distance plots and corresponding SEM images at constant normal load of (a) 2000 μN , (b) 4000 μN and (c) 8000 μN . (d) 2D cross-sectional profile of micro-scratches and (e) wear volume (scratch volume) at different normal loads.

figure for representative scratches at each load showing (i) SPM image of the scratch, (ii) lateral displacement vs. COF/lateral force plots and (iii) corresponding SEM image of the scratch in the same scale length. The SPM images in Fig. 2 (the same scale) show the increasing width of the scratch with an increasing normal load, which also indicates the increase in the depth derived from the pyramidal shape of the Berkovich indenter. Corresponding SEM images in the same figures also corroborate the observations from SPM images.

Lateral displacement vs. COF/lateral force plot shows drops at 4000 and 8000 μN normal loads (Fig. 2b and c), whereas such features are absent at 2000 μN (Fig. 2a). The drops in the lateral force indicate incidents of fracture and chipping. At the onset of a fracture or chipping, the scratch probe gets unbalanced and loses its support, thus incurring a large drop in the lateral force. At the next moment, due to the surface roughness created by fracture/chipping and the presence of loosened debris, the lateral force required to move goes high. Thus, any drop in the plot is also associated with a small sharp hump just following, in the lateral force vs. distance plots (Fig. 2b and c). The presence of large drops in Fig. 2b and c, and its absence in Fig. 2a reveal that the critical “lateral” force for chipping to occur is between 600 and 800 μN . A larger drop in the lateral force is observed at 8000 μN normal load (Fig. 2c),

indicating aggravated fracture and chipping. The COF is ~ 0.2 at 2000 μN and increases to a range of ~ 0.3 – 0.4 at 4000 μN and 8000 μN , respectively (Fig. 2). Increasing amount of roughening and debris generation on the surface due to fracture and chipping explains the increase in COF with normal load. Though the fracture and chipping indicate domination of brittle behavior, still some plastic deformation is expected. Thus increase in COF can also have some contribution from increasing plastic deformation at higher normal load. SEM images in Fig. 2a also reveal smooth banks of the scratch at 2000 μN ; whereas, signs of chipping and fracture are obvious at the higher loads (Fig. 2b and c). These findings are similar in nature to the previous reports on Mg-, Zr-, Cu- and Ni-rich metallic glasses, where scratches were made with constant normal loads in the range of μN – mN [12,14–16]. The increase in COF with an increasing load is largely attributed to fracture and chipping, which also explains a larger variation of the same. The small serrations in the lateral force and COF curves are potentially due to the shear band formation which is elaborated in Section 3.6. Note that, the almost negligible serration at 2000 μN is suggestive that deformation occurs by ductile plowing. The mode of deformation changes to fracture and shear band formation at 4000 μN , which is indicated by large drops and small serrations, respectively, in the lateral force. A similar change

in the deformation mode from ductile to shear localization and chipping is noted for hard BMGs [20]. The amplitude and spacing of the serrations observed at 4000 μN increase at 8000 μN normal load.

Fig. 2d presents the representative 2-D cross-sectional profiles of scratches at different normal loads, obtained from SPM images.

The pile-up volume is 2.6–3.2 times greater than the scratch groove volume which suggests a high degree of localized free volume generation (Fig. 2d). This is most likely achieved by the strain accommodation by shear band assisted deformation. Wear volume for three loads is evaluated by measuring the volume of the scratch grooves from SPM images. Wear volumes presented in Fig. 2e show a significant 170% increase from 2000 μN to 4000 μN . But the increase is not linear at 8000 μN , which is only 35% over 4000 μN . The sharp increase in the wear volume at 4000 μN is due to the change in deformation mode from ductile to fracture/chipping domination.

3.3. Micro-scratch: ramped loading

Micro-scratches were also made by ramping the normal load between 0 and 8000 μN along a scratch length of 10 μm . These scratches were made to compare and evaluate if the deformation mechanism in ramp loading is different from constant loading mode. Scratches made at ramp load experience difference in the loading rate, and consequently, strain rate, along each point of the scratch. Hence, this set of experiments is also referred as dynamic loading. Fig. 3 provides a composite view of a scratch in ramp loading. The COF remains relatively similar throughout the scratch length, indicating no pile-up or strain hardening (Fig. 3). The absence of large drops in lateral force plot indicates minimal fracture or chipping. This observation from the COF plot is corroborated

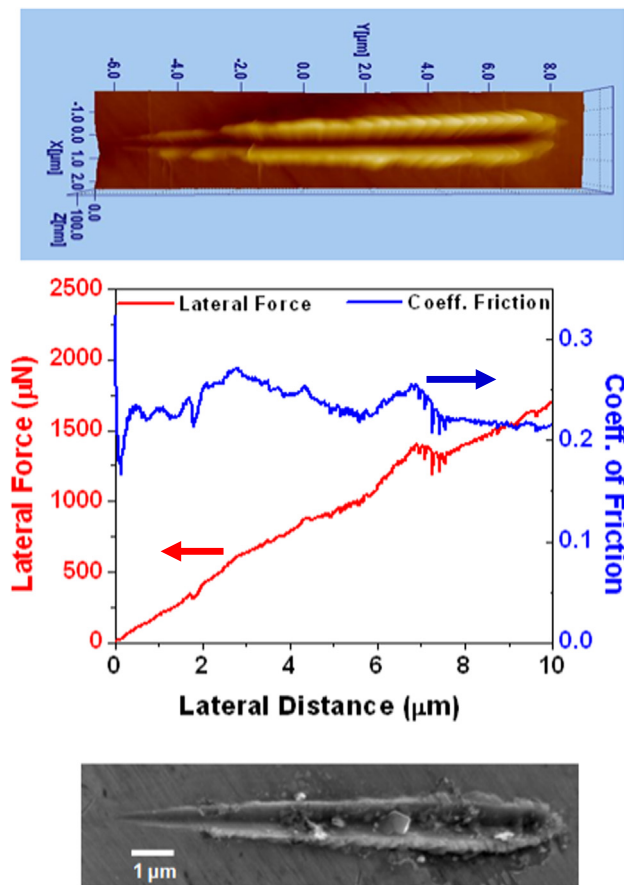


Fig. 3. SPM image, lateral force and coefficient of friction vs. scratch distance plot and SEM image of micro-scratch made at ramp loading with normal load range of 0–8000 μN .

by the SEM micrograph of the corresponding scratch presented in Fig. 3, revealing minimal sign of fracture and chipping in the groove.

The reduction in fracture and chipping causes lower COF of 0.2–0.25 over the entire loading range (Fig. 3). In contrast, the constant load results show the COF in the range of 0.3–0.4 at higher loads, due to significant fracture and chipping (Fig. 2b and c). Less risk of fracture and chipping in ramp loading is possibly attributed to accelerated shear band formation, which can accommodate more plastic deformation without chipping. Local perturbation in strain rate is responsible for the origin of shear bands, which makes nucleation of shear bands easier during ramp loading [22]. High magnification SEM micrographs presented in Fig. 4 also agree with this fact by revealing more prominent and distinguishable shear bands at the bank of ramp-loaded scratch (Fig. 4b), as compared to the constant-loaded one (Fig. 4a). Shear band formation leads to localized free volume generation. Thus, the free volume generation should be more in the case of ramped loading. The next section discusses free volume generation and deformation behavior of the Hf-BMG as a function of ramp vs. constant loading mode.

3.4. Micro-scratch: comparison of deformation between constant and ramped loading

Profiles across the scratch grooves under ramp loading were captured from SPM images at three different points where the normal load corresponds to 2000, 4000 and 8000 μN . Fig. 5 presents comparative profiles of scratch grooves for constant and ramp loading at three different loads. The profile of scratch groove at 8000 μN for ramp loading (Fig. 5c) is approximated as the actual point, which was at the tip of the groove. Scratch groove is slightly deeper in ramp loading for three loads, which denotes more plastic deformation. But the difference is more at 2000 μN (Fig. 5a) and becomes less for 4000 μN and 8000 μN (Fig. 5b and c). The probable reason for such behavior is significant fracture and chipping in higher constant load scratches (4000 and 8000 μN), which reduces the chance of elastic recovery and the scratch groove remains deeper.

The free volume generation in each case is presented by the ratio of area under pile-ups and scratch groove (schematic shown in Fig. 2d), which indicates post-deformation volume increase in the Hf-BMG. Fig. 5d presents pile-up/groove volume ratio for the constant and ramped load scratches at 2000, 4000, and 8000 μN normal load. In the case of constant loading, the free volume generation decreases marginally with an increasing normal load due to the contribution from fracture and chipping in scratch volume. Note that, the free volume generation is higher in the case of ramp loading at each of the normal loads. This observation supports the discussion in the previous Section 3.3 on the ease of shear band nucleation due to dynamic strain rate under ramped loading conditions. The free volume generation rate during ramping increases from 2000 μN to 4000 μN , which is opposite to the behavior noted at constant load. This was possible due to the absence of significant fracture and chipping as well as higher strain rate change making shear band assisted plastic deformation easier. The SEM image in Fig. 4b also furnishes the visual proof of more distinguishable shear band formation along the bank of the groove with the progression of scratch in ramped loading. On the contrary, less increase in free volume generation rate is noted at 8000 μN for ramp load. It is attributed to a combination of factors: (i) it was not possible to collect the profile exactly at 8000 μN for ramp loading as it was at the end of the scratch, (ii) strain hardening at higher load [22] and (iii) possible chipping at highest load. The increase in volume due to oxygen incorporation in the material can be neglected considering the fact that Hf-based BMG should possess insignificant reactivity at room temperature.

3.5. Macro-scratch: ramped loading

Scratches were also made at much higher ramp loads of 0–5 N to understand the deformation behavior of the Hf-BMG. Scratches of 1.5 mm

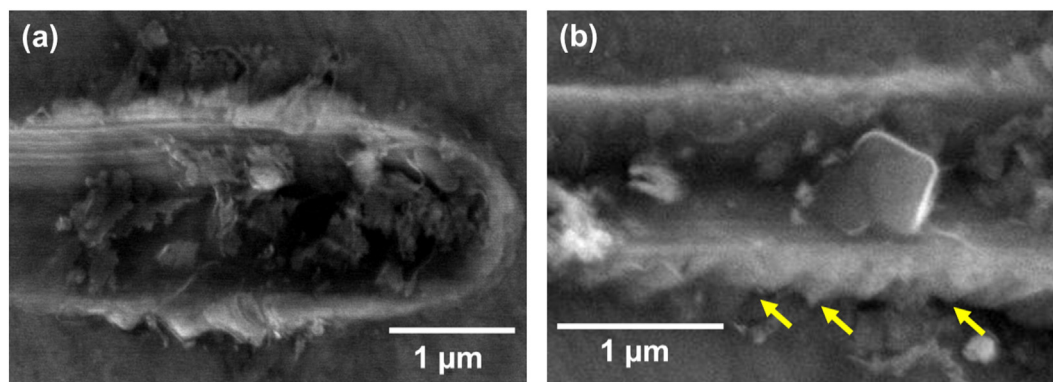


Fig. 4. SEM images of micro-scratch at (a) 8000 μN constant load and (b) 0–8000 μN ramp load showing fractured chips, linear plowing mark in the scratch groove, and shear band formation at the edge (marked by arrows).

length were made with cono-spherical diamond probe of 50 μm tip-radius. The load applied for these scratches is 1000 times greater than in the ramped micro-scratches discussed earlier. The residual depth of these scratches is up to 1.5 μm , which is ~ 20 times more than that of micro-scratches. Hence, these scratches are referred as macro-scratches in this study. A composite visual of the optical image, lateral displacement vs. COF/lateral force, and SEM image of a macro-scratch is presented in Fig. 6. The initial part of the COF plot shows a lot of noise/disturbance, which could be due to the low loads at the beginning that fails gripping by the cono-spherical tip on the glassy surface due to the high resilience/hardness of the BMG surface. In contrast to the micro-scratches (Fig. 3), the COF is found to increase along the macro-scratch length (Fig. 6). At the same time, the large drops in the lateral force, which indicates fracture/chipping events, do not increase significantly in magnitude with an increasing normal load. This implies that

the increase in COF cannot be solely due to increasing fracture and chipping. Instead, the increase in COF is likely more dominated by increasing plastic deformation and associated strain hardening in the macro-scratch track as compared to micro-scratch. This observation suggests a significantly higher strain-hardening effect during macro-scratching than micro-scratching, as the COF remains similar with increasing load in the latter. A common way of strain hardening in BMGs is by nano-crystal formation [22,23]. Localized heating could be a probable cause for the nucleation of nano-crystals in shear bands. This will be explained in Section 3.6 in more detail.

However, researchers have suggested that localized heating cannot be the sole cause for crystallization in shear bands as it is observed even when the temperature rise is very small [24,25]. Evolution/formation of nano-crystals in BMG is also observed as a result of high strain rate that causes non-Newtonian deformation [26–28]. The scratch velocity is

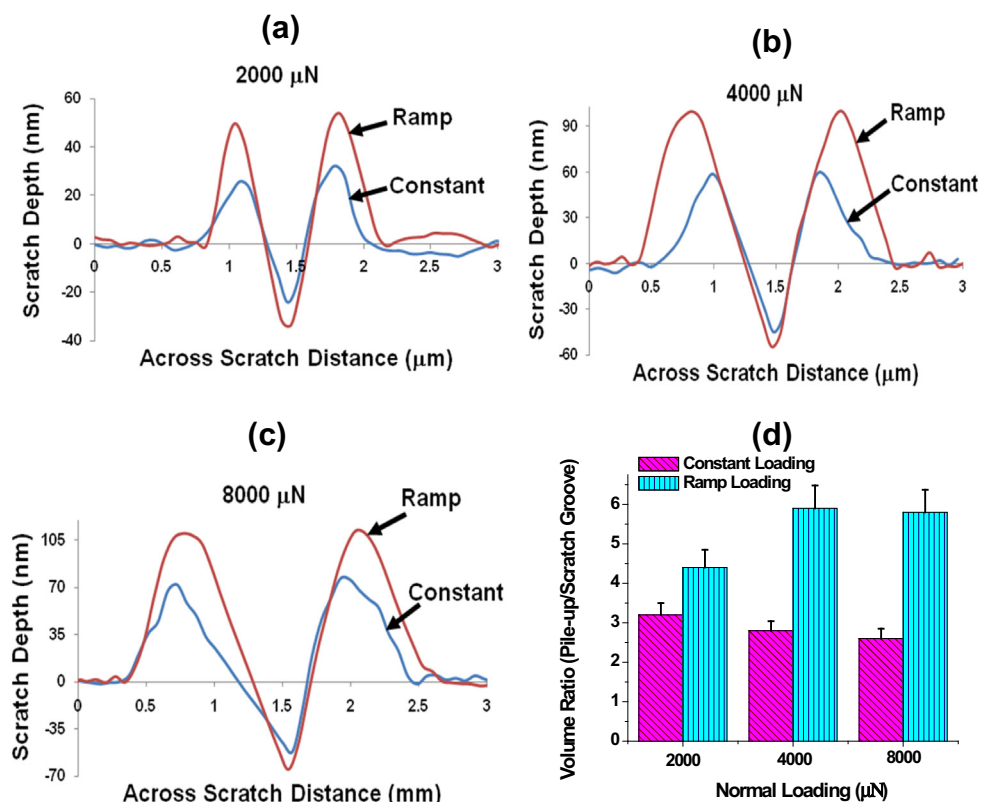


Fig. 5. Comparative scratch groove profiles of constant and ramped loading at similar normal loads of (a) 2000 μN ; (b) 4000 μN and (c) 8000 μN . (d) Pile-up to groove volume ratio for micro-scratches at constant and ramp load.

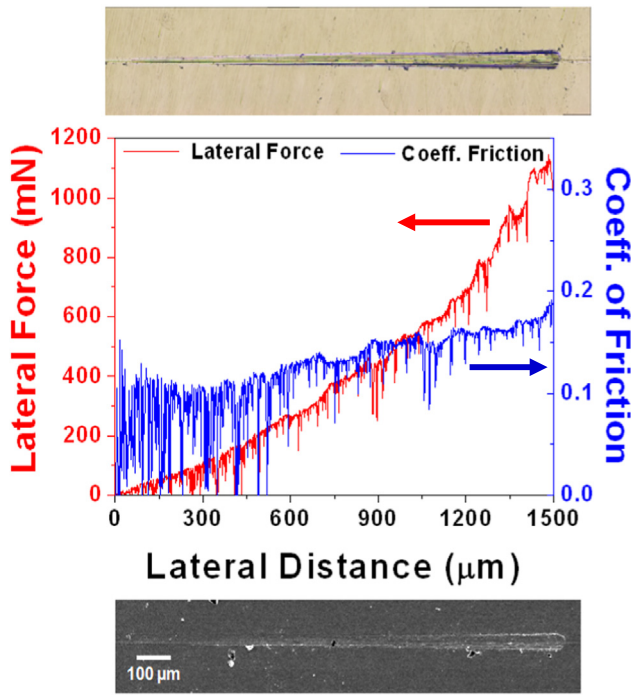


Fig. 6. Optical image, lateral force and coefficient of friction vs. scratch distance plot and SEM image of macro-scratch made at ramp loading with normal load range of 0–5 N.

$1 \mu\text{m}\cdot\text{s}^{-1}$ for micro-scratch and $8.33 \mu\text{m}\cdot\text{s}^{-1}$ for macro-scratch. The strain rate is ~ 8 times more in macro-scratch, which provides higher possibility for forming nano-crystals as compared to micro-scratch. Moreover, nano-crystal formation is more preferred in compression than in tension [29]. The normal load applied in scratching is also compressive in nature, which will assist in the nucleation of nano-crystals in the shear bands generated. In turn, the nano-crystals, present in shear bands could increase the flow stress effectively, leading to strain hardening and initiation of new shear band to accommodate the strain.

Fig. 7 presents the SEM images of different regions of a macro-scratch. The micrographs present prominent features of the scratch at macro-scale. e.g., absence of pile-up at the end of scratch, two types of shear bands at the edge, and sign of melting on the scratch groove. The authors believe that this dual type of shear bands are formed as a result of scratch based deformation in BMGs, irrespective of the loading range, and should also be featured in the edge of micro-scratches. But, due to much lower level of loading, they could not be resolved in the micrographs.

Scratch-based deformation is significantly different and more complex than deformation based on normal indentation alone, as it involves simultaneous application of two types of load, viz. a compressive load acting normal to the surface and lateral shearing load acting parallel to the surface. Considering the fact that deformation in BMGs is mostly accommodated by shear band formation, the two types of loading during scratch are supposed to generate two different sets of shear bands. A closer and more careful observation at the edge of macro-scratches reveals two sets of shear bands oriented at different angles to the track (Fig. 7c). A magnified view of the region is presented in Fig. 8a, which

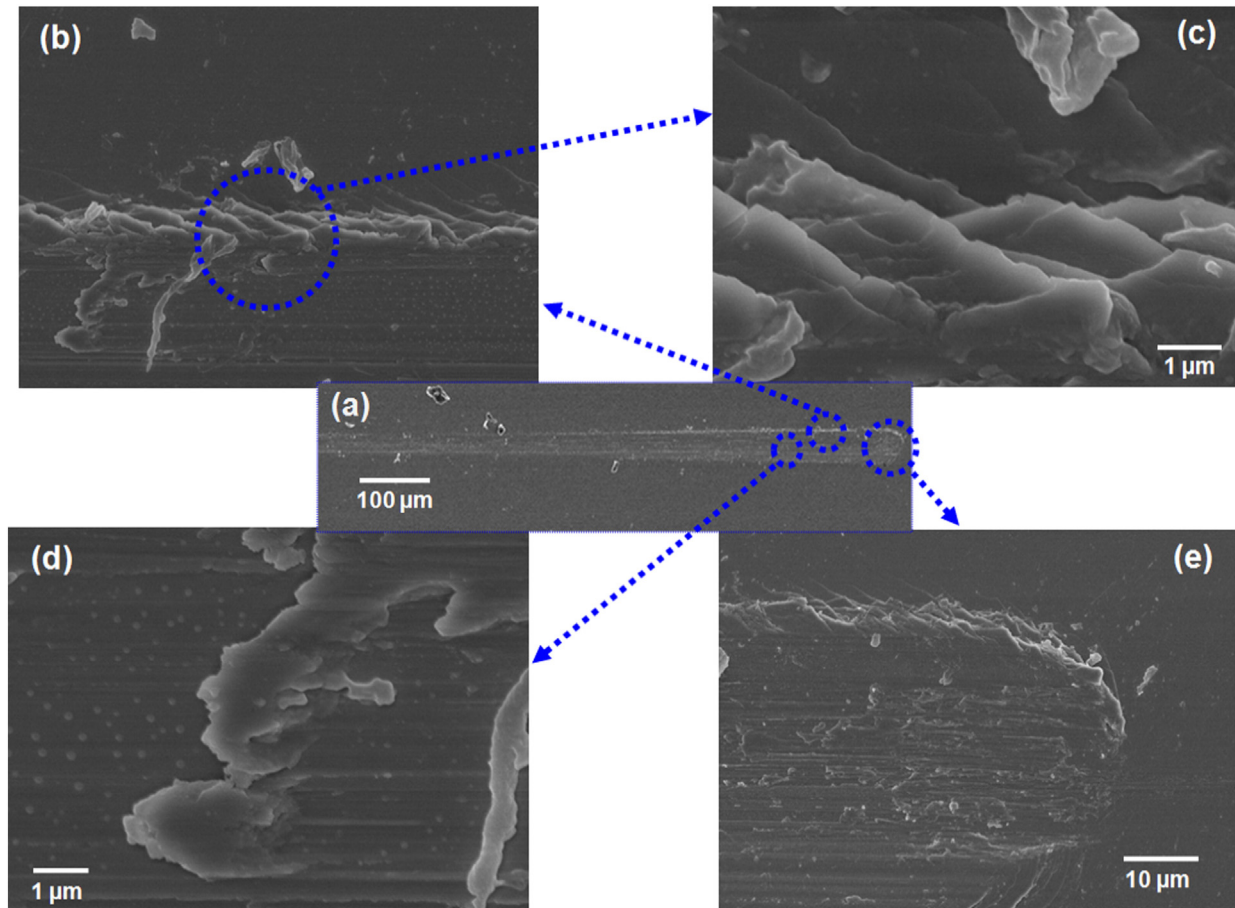


Fig. 7. SEM images of macro-scratch at 0–5 N ramp load showing (a) the full scratch; (b–c) the shear band formation at the edge of scratch groove at different magnifications; (d) scratch groove with fractured chips showing sign of melting; (e) clean tip of the scratch showing absence of pile-up due to slip related plastic deformation.

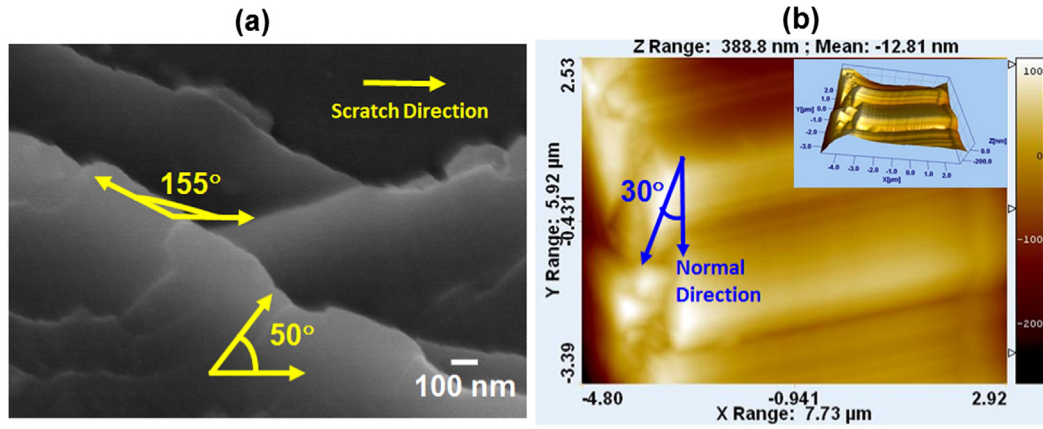


Fig. 8. (a) SEM image of the shear band region at the edge of macro-scratch groove $\sim 70\text{--}80\text{ }\mu\text{m}$ away from the tip, showing the two sets of shear bands with respect to the direction of shear loading. The bands at 50° in SEM image are generated from shear loading whereas shear bands at 155° are caused by normal compressive loading (b) SPM image of the same region showing 30° angle between normal compressive loading direction and associated shear bands.

shows a set of pronounced shear bands at $\sim 150^\circ$ to the scratch direction. Another set of fine shear bands are found on making $\sim 50^\circ$ with the scratch direction. Similar observations were made by Subhash and Zhang during dynamic scratching of Zr-based BMGs [13]. The origin of the complex shear band structure was attributed to the dual mode of loading during scratch, though no analysis was presented to correlate the structure with type of loading [13]. In the present study, we have made an attempt to correlate the shear band patterns with the type of loading.

The COF for macro-scratch varies between 0.1 and 0.2, which implies that the normal loads are at least 5 times higher than the lateral force at any point in the track. Thus, the strain associated with normal load would need wider and larger shear bands as compared to strain from the lateral load. As a consequence, the more prominent shear bands at $\sim 150^\circ$ to the scratch direction should be due to normal loading, while the origin of finer ones at $\sim 50^\circ$ is from shear loading. Subhash and Zhang have also observed through the bonded cylindrical specimen method that the shear bands originated at the tip of scratch probe propagates to the top surface with similar band spacing [13]. Thus, it is possible to observe the shear bands from normal loading to the bank of the scratch groove of the sample. It is also possible to correlate the angle that shear bands make with loading axis (θ) with deformation by means of coefficient of normal stress dependence (α_n), which is also defined as coefficient of friction of shear transformation zone (STZ) operation [22]. The relationship is as follows:

$$2\theta = \cot^{-1}(\alpha_n) \text{ in compression and} \quad (1)$$

$$2\theta = \cot^{-1}(-\alpha_n) \text{ in tension.}$$

The angle between the normal load direction and associated shear bands cannot be calculated from the surface profiles, as the direction of normal load is perpendicular to sample surface. Thus, scanning probe imaging of the scratch edge was carried out to find the angle (Fig. 8b). The angle between lateral load and associated shear bands is estimated from SEM images (Fig. 8a).

Taking the ramp type of loading into consideration, both calculations are done at the same position of the scratch, at $\sim 70\text{--}80\text{ }\mu\text{m}$ away from the scratch tip, to keep the loading conditions similar. The angle between normal force and the associated shear bands is found to be $\sim 30^\circ$ (Fig. 8b), whereas the same for lateral force is $\sim 50^\circ$ (Fig. 8a). The normal force is compressive in nature, whereas the shearing nature of lateral force causes an elongation type of deformation on the top layers of scratch surface, which could be assumed equivalent to a tensile condition. Calculations using Eq. (1) reveal α_n to be 0.58 for normal load and 0.18 for lateral load. Both the α_n values come out to be positive

and COF for STZ operation cannot be negative. Thus, the correspondence of shear bands with loading type is justified, as the opposite assignment can result in negative values for COF of STZ operation. In addition, α_n for normal compressive load is ~ 3 times higher than that associated with lateral load in the track. This could be expected due to ~ 5 times higher magnitude of normal load as compared to lateral force.

The serrations in lateral force plots for micro- and macro-scratches (Figs. 2, 3 and 6) are correlated to the origin of individual shear bands. The width of small serrations in lateral force plot of macro-scratch is measured and compared with the width of shear bands in SEM image (Fig. 9a). Similar position along the length of the scratch ($\sim 70\text{--}80\text{ }\mu\text{m}$ away from the scratch tip) is chosen, as the ramped load would cause progressive change in width of the shear bands. The spacing between lateral force originated shear bands is $550\text{--}700\text{ nm}$ (Fig. 9a). The undulations of the lateral force plot also have a period of $\sim 900\text{ nm}$ (Fig. 9b). Considering the spatial resolution of linear force data points as $833\text{ }\mu\text{m}$, the spacing of undulations in the lateral force plot is approximated to be in similar range as the spacing of shear bands. This observation corroborates that small serrations in lateral force are due to the origin of new shear bands.

3.6. Macro-scratch vs. micro-scratch: difference in deformation behavior

A comparison of high magnification micrographs from macro- (Fig. 7) and micro-scratches (Fig. 4) reveals the comparative features of deformation in the Hf-based BMG at different length scales. Scratches at both scales reveal the absence of pile-ups at the scratch tip (Figs. 7e and 4a). However, pile-up at edges with clear signs of band formation is observed at both scales of load (Figs. 7b–c and 4a–b). Thus, it is concluded that the plastic strain in both cases is accommodated by shear localization, which is a signature feature of BMG structures. Scratch tracks show linear marks indicating plowing of material by probe for both cases (Figs. 7d–e, and 4a). The presence of chips and flakes in the micro-scratch track, compared to the smoother track in the macro-scratch implies more brittle fracture and failure type material loss in the former (Figs. 7 and 4). The use of the sharper pyramidal Berkovich probe during micro-scratch is found to be responsible for more fracture and chipping as compared to the rounded surface of the spherical probe used during macro-scratch. In addition, less fracture and chipping during macro-scratch might be due to accommodation of strain and absorption of related energy with increased plastic flow. Prasad and Ramamurty have observed more plastic flow in BMGs with higher temperature, which drives large number of STZ movements and forms wider shear bands [30]. More heat evolution in the macro-scratch groove is evident from the molten type features of the partially delaminated material as observed in Fig. 7d. Localized heat generation

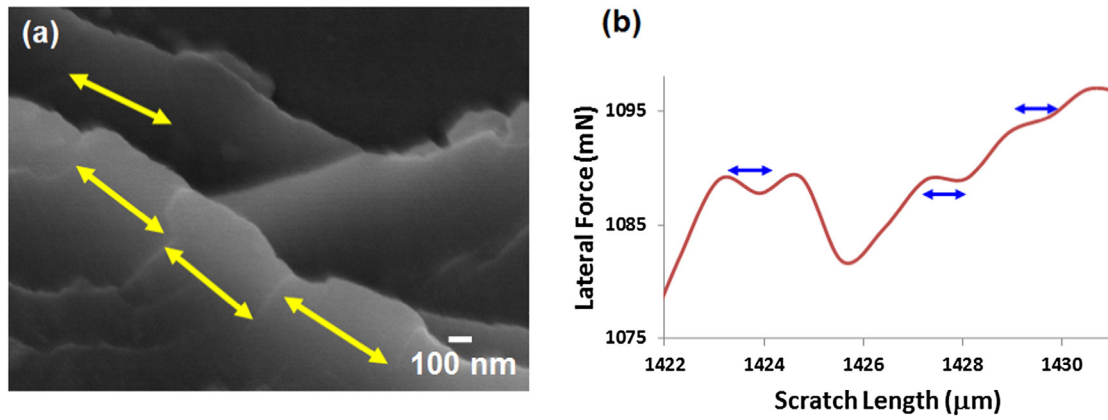


Fig. 9. (a) The width of the lateral force created shear bands at the edge of macro-scratch shear bands is marked with arrows and (b) corresponding lateral force vs. scratch length plot of macro-scratch from the same region of SEM micrograph in (a) showing width of the serrations/undulations in the load.

in the macro-scratch groove due to sliding contact with the probe can cause partial melting in the track. Such features are not found in micro-scratch groove. A semi-quantitative calculation based on existing models has been carried out to estimate the comparative heat evolution in the scratches. The increase in temperature (ΔT) of the sample surface due to scratching is estimated using a relationship for sliding of contact surfaces proposed by Ashby [31–33] as follows:

$$\Delta T = (T_s - T_0) = \frac{\mu F_N V}{A_n} \frac{1}{\frac{K_a}{l_a} + \frac{K_b}{l_b}} \quad (2)$$

where, T_s and T_0 are the surface contact and reference (bulk material) temperatures, respectively. Further, F_N is the normal force, V is the velocity, A_n is the contact area, and μ is the COF of sliding contact; K_a and K_b are the thermal conductivities of sample and probe and the 'l' terms denote respective equivalent linear diffusion distances. The last terms in Eq. (3), consisting of K and l for the sample and probe remain similar in both macro- and micro-scratch conditions. This is because the probe used is made of diamond in both situations. Thus, Eq. (3) can be modified as follows for the present study.

$$\Delta T = C \frac{\mu F_N V}{A_n} \quad (3)$$

In Eq. (4), C is a constant, which is the same for macro- and micro-scratch. The temperature increase is computed for three positions in each track, chosen with a normal load taken into consideration. The three points on both types of tracks were chosen to compare the temperature rise in the track at three proportional loading positions, normalized with the peak load. The three loads during ramped micro-scratch are 2000, 4000 and 8000 μ N. The three points on macro-scratch were selected at proportional normalized loads of 1.25, 2.5 and 5 N. The COF is also determined at the selected loads in the scratch track. The contact area of the probe is calculated by determining the depth of penetration with the selected loads and using the established relationships for the type of probes used. The maximum penetration depth in the case of macro-scratch is $\sim 7 \mu$ m, whereas the radius of the cono-spherical probe is 50μ m. Thus, the probe can be assumed as spherical with respect to the depth of penetration. The contact area of a spherical indenter probe can be expressed as [34]:

$$A_n = \pi(2R_i h_p - h_p^2) \approx 2\pi R_i h_p \quad (4)$$

where, R_i is the radius of indenter and h_p is the depth of penetration. For micro-scratch, the contact area is calculated from the calibration plot of the Berkovich tip used for these studies, to take care of the bluntness, if

any, introduced by the probe. The polynomial expression of the contact area of the probe as a function of penetration depth is as follows:

$$A_n = 24.5h_p^2 + 7.5419 \times 10^3 h_p - 3.8776 \times 10^5 h_p^{1/2} + 3.8123 \times 10^6 h_p^{1/4} - 9.7183 \times 10^6 h_p^{1/8} + 6.3676 \times 10^6 h_p^{1/16} \quad (5)$$

The $C \cdot \Delta T$ at the three points in each of the macro- and micro-scratches are presented in Table 1. Since C is constant for all the cases, the increase in this parameter can be directly related to the increase in temperature, ΔT . The macro-scratch shows 2.7–7 times greater temperature increase at the respective distances along the scratch track, as compared to micro-scratch. Such high temperature exposure easily leads to nano-crystal formation in the macro-scratch [22,35] and possible localized melting as observed in Fig. 7d. The combination of the effect of higher temperature generation and more strain in macro-scratch leads to significantly higher nano-crystallite formation. Furthermore, nanocrystallization results into strain hardening in the macro-scratch, which is evident from the increase in COF (Fig. 6). Conversely, the lack of nanocrystallization in micro-scratch explains the absence of strain hardening and no increase in COF (Fig. 3).

4. Conclusions

This study presents the scratch-based deformation behavior of a Hf-based BMG with the composition of $\text{Hf}_{46.29}\text{Cu}_{28.19}\text{Ni}_{13.91}\text{Al}_{6.19}\text{Nb}_{5.42}$. Constant load micro-scratch studies reveal a transformation of the deformation from plowing to fracture and chipping with an increasing normal load. The absence of pile-up of materials at the tip of scratch and prominent shear bands at the bank of scratches is observed. A 2.6–3.2 times of free volume generation is observed in the surface profiles across the scratch. Micro-scratch under ramp load shows reduced fracture and chipping and larger free volume generation than those under constant load. Shear band nucleation is easier in ramp loading and, thus, helps in accommodating more plastic strain. Micro-scratches show constant COF with increasing load whereas the COF increases for

Table 1

Estimated increase in the temperature for scratches at macro- and micro-scale made with ramp load (C is a constant).

	Normal load (N)	$C \cdot \Delta T$
Macro-scratch	1.25	1890 ± 205
	2.5	2650 ± 256
	5	4080 ± 385
Micro-scratch	0.002	750 ± 79
	0.004	690 ± 68
	0.008	570 ± 53

macro-scratches. This behavior suggests that more strain hardening occurs in the case of macro-scratch. Higher strain rate and more heat generation in the case of macro-scratch can possibly lead to nanocrystallization in shear bands, which assists in further strain hardening. Two different sets of shear bands are formed at the bank of scratches, due to simultaneous application of normal and shear loads. The small serrations in the lateral force plot are correlated with the width of shear bands which are generated to accommodate lateral strain.

Acknowledgment

AA and DL acknowledge support of AMERI at FIU, in maintaining and providing the research facilities. The authors acknowledge the help from Prof. Todd C. Hufnagel at Johns Hopkins University for synthesizing Hf based BMG samples. GSD and AA also acknowledge the research grant W911NF-06-1-0328 from US Army Research Office.

References

- [1] X. Gu, L.Q. Xing, T.C. Hufnagel, Glass-forming ability and crystallization of bulk metallic glass ($\text{Hf}_{52}\text{Zr}_{1-x}\text{Cu}_{17.9}\text{Ni}_{14.6}\text{Al}_{10}\text{Ti}_5$), *J. Non-Cryst. Solids* 311 (2002) 77–82.
- [2] X. Gu, T. Jiao, L.J. Kecskes, R.H. Woodman, C. Fan, K.T. Ramesh, T.C. Hufnagel, Crystallization and mechanical behavior of (Hf, Zr)–Ti–Cu–Ni–Al metallic glasses, *J. Non-Cryst. Solids* 317 (2003) 112–117.
- [3] L. Zhang, L.-L. Shi, J. Xu, Hf–Cu–Ni–Al bulk metallic glasses: optimization of glass-forming ability and plasticity, *J. Non-Cryst. Solids* 355 (2009) 1005–1007.
- [4] T.D. Krus, T.F. Juliano, L.J. Kecskes, M.R. VanLandingham, Initial plasticity onset in Zr- and Hf-rich bulk metallic glasses during instrumented indentation, *J. Mater. Res.* 22 (2007) 1265–1269.
- [5] L.C. Damonte, L. Mendoza-Zelis, Crystallization steps in Zr- and Hf-based bulk metallic glasses, *J. Alloys Compd.* 434–435 (2007) 244–247.
- [6] G. Subhash, H. Zhang, Dynamic indentation response of ZrHf-based bulk metallic glasses, *J. Mater. Res.* 22 (2007) 479–485.
- [7] A. Revesz, J.-L. Uriarte, D. Louzguine, A. Inoue, S. Surinach, M.D. Baro, A.R. Yavari, Thermal properties of Hf-based metallic glasses, *Mater. Sci. Eng. A* 375–377 (2004) 381–384.
- [8] N. Nikolov, A.R. Yavari, Investigations on glass forming ability of Hf-alloys by mathematical modeling and optimizations, *Mater. Trans. Japan. Inst. Met.* 44 (2003) 1752–1759.
- [9] D.R. Maddala, A. Mubarak, R.J. Hebert, Sliding wear behavior of $\text{Cu}_{50}\text{Hf}_{41.5}\text{Al}_{8.5}$ bulk metallic glass, *Wear* 269 (2010) 572–580.
- [10] N. Togashi, M. Ishida, N. Nishiyama, A. Inoue, Wear resistance of metallic glass bearings, *Rev. Adv. Mater. Sci.* 18 (2008) 93–97.
- [11] M.Z. Ma, R.P. Liu, Y. Xiao, D.C. Lou, Q. Wang, W.K. Wang, Wear resistance of Zr-based bulk metallic glass applied in bearing rollers, *Mater. Sci. Eng. A* 386 (2004) 326–330.
- [12] C.T. Pan, T.T. Wu, J.K. Tseng, C.Y. Su, W.J. Wang, J.C. Huang, Mechanical behavior of metallic glasses Mg–Cu–Y using nanoindentation, *Microsyst. Technol.* 16 (2010) 585–593.
- [13] G. Subhash, H. Zhang, Shear band patterns in metallic glasses under static indentation, dynamic indentation, and scratch processes, *Met. Mater. Trans. A* 38A (2007) 2936–2942.
- [14] B. Sun, Z. Zhan, Indentation and friction of $\text{Cu}_{44}\text{Zr}_{43}\text{Al}_{10}\text{Nb}_3$ bulk metallic glasses on nano-scale, *Appl. Mech. Mater.* 130–134 (2012) 2750–2753.
- [15] S. Yoon, C. Lee, H. Choi, Evaluation of the effects of the crystallinity of kinetically sprayed Ni–Ti–Zr–Si–Sn bulk metallic glass on the scratch response, *Mater. Sci. Eng. A* 449–451 (2007) 285–289.
- [16] M.Z. Ma, H.T. Zong, H.Y. Wang, W.G. Zhang, A.J. Song, S.X. Liang, Q. Wang, X.Y. Zhang, Q. Jing, G. Li, R.P. Liu, Indentation and friction of Zr-based bulk metallic glasses on nano-scale, *Mater. Lett.* 62 (2008) 4348–4350.
- [17] Y. Huang, Y.L. Chiu, J. Shen, Y. Sun, J.J. Chen, Mechanical performance of metallic glasses during nanoscratch tests, *Intermetallics* 18 (2010) 1056–1061.
- [18] C.T. Pan, T.T. Wu, C.F. Liu, C.Y. Su, W.J. Wang, J.C. Huang, Study of scratching Mg-based BMG using nanoindenter with Berkovich probe, *Mater. Sci. Eng. A* 527 (2010) 2342–2349.
- [19] A.M. Hodge, T.G. Nieh, Evaluating abrasive wear of amorphous alloys using nanoscratch technique, *Intermetallics* 12 (2004) 741–748.
- [20] J. Michler, R. Rabe, J.-L. Bucaille, B. Moser, P. Schwaller, J.-M. Breguet, Investigation of wear mechanisms through in situ observation during microscratching inside the scanning electron microscope, *Wear* 259 (2005) 18–26.
- [21] M.D. Abramoff, P.J. Magelhaes, S.J. Ram, Image processing with ImageJ, *J. Biophoton. Int.* 11 (2004) 36–42.
- [22] C.A. Schuh, T.C. Hufnagel, U. Ramamurty, Mechanical behavior of amorphous alloys, *Acta Mater.* 55 (2007) 4067–4109.
- [23] M. Chen, A. Inoue, W. Zhang, T. Sakurai, Extraordinary plasticity of ductile bulk metallic glasses, *Phys. Rev. Lett.* 96 (2006) 245502.
- [24] J.-J. Kim, Y. Choi, S. Suresh, A.S. Argon, Nanocrystallization during nanoindentation of a bulk amorphous metal alloy at room temperature, *Science* 295 (2002) 654–657.
- [25] W.H. Jiang, F.E. Pinkerton, M. Atzmon, Effect of strain rate on the formation of nanocrystallites in an Al-based amorphous alloy during nanoindentation, *J. Appl. Phys.* 93 (2003) 9287–9290.
- [26] T.G. Nieh, J. Wadsworth, C.T. Liu, T. Ohkubo, Y. Hirotsu, Plasticity and structural instability in a bulk metallic glass deformed in the supercooled liquid region, *Acta Mater.* 49 (2001) 2887–2896.
- [27] T.G. Nieh, C. Schuh, J. Wadsworth, Y. Li, Strain rate-dependent deformation in bulk metallic glasses, *Intermetallics* 10 (2002) 1177–1182.
- [28] B.-G. Yoo, I.-C. Choi, Y.-J. Kim, J.-Y. Suh, U. Ramamurty, J.-I. Jang, Further evidence for room temperature, indentation-induced nanocrystallization in a bulk metallic glass, *Mater. Sci. Eng. A* 545 (2012) 225–228.
- [29] W.H. Jiang, M. Atzmon, The effect of compression and tension on shear-band structure and nanocrystallization in amorphous $\text{Al}_{90}\text{Fe}_5\text{Gd}_5$: a high-resolution transmission electron microscopy study, *Acta Mater.* 51 (2003) 4095–4105.
- [30] K.E. Prasad, U. Ramamurty, Effect of temperature on the plastic zone size and the shear band density in a bulk metallic glass, *Mater. Sci. Eng. A* 535 (2012) 48–52.
- [31] M.F. Ashby, J. Abulawi, H.S. Kong, Temperature maps for frictional heating in dry sliding, *Tribol. Int.* 34 (1991) 577–587.
- [32] S. Wilson, A.T. Alps, Thermal effects on mild wear transitions in dry sliding of an aluminum alloy, *Wear* 225–229 (1999) 440–449.
- [33] G. Straffelini, A. Molinari, Dry sliding wear of Ti–6Al–4V alloy as influenced by the counterface and sliding conditions, *Wear* 236 (1999) 328–338.
- [34] A.C. Fischer-Cripps, Nanoindentation, Springer-Verlag, New York, 2004, ISBN 0-387-22045-3.
- [35] A.A. Csontos, G.J. Shiflet, Formation and chemistry of nanocrystalline phases formed during deformation in aluminum-rich metallic glasses, *Nanostruct. Mater.* 9 (1997) 281–289.